GeoScienceWorld
Lithosphere
Volume 2024, Article ID lithosphere_2023_314, 16 pages
https://doi.org/10.2113/2024/lithosphere_2023_314

Lithosphere

Research Article

Compressive Fracture Behavior and Acoustic Emission Characteristics of Sandstone under Constant Crack Water Pressure

Jiancheng Huang,[1] Yong Luo,[1,2] Chengzhi Pu,[1] Song Luo,[3] and Xuefeng Si[1]

[1]*School of Resources Environment and Safety Engineering, University of South China, Hengyang, 421001, China*
[2]*Chinalco Zhongzhou Mining Co., Ltd., Jiaozuo, 454174, China*
[3]*School of Resources and Safety Engineering, Central South University, Changsha, 410083, China*

Correspondence should be addressed to Song Luo; luosong@csu.edu.cn

Received 21 October 2023; Accepted 30 January 2024; Published 16 February 2024

Academic Editor: Zijun Fang

Engineering rock containing flaws or defects under a large water source is frequently subject to the couple influence of constant crack water pressure and geostress. To investigate the fracture behavior of precracked rock under hydromechanical coupling with constant crack water pressure, compression tests were conducted on red sandstone specimens containing a single crack of different angles using a device to realize the constant crack water pressure during loading, and the failure process of rock specimens was monitored by acoustic emission (AE) technique. The results show that the presence of constant crack water pressure has a significant promotion effect on the development of shear wing cracks, and the promotion effect is influenced by the prefabricated crack angle and water pressure. As the constant crack water pressure increases, the failure mode of the 0° precrack specimen changes from "X"- shear failure to the single oblique shear failure along the shear wing crack direction, the main failure crack of the inclined precracked specimens (precrack angles of 15°, 45°, and 60°) changes from a small acute angle with the prefabricated crack to a direction along the shear wing crack, and irregular cracks occur at the chipped prefabricated crack in the 90° precracked specimen. With an increase in the constant crack water pressure, the average energy for a single hit, cumulative AE energy, and cumulative AE hits decrease, and the proportion of the tensile cracks increases and that of the shear cracks decreases.

1. Introduction

In underground mining, water conservancy and hydropower, geothermal development, and oil exploitation projects, rock structure inevitably contains various flaws and can be damaged and destroyed due to stress variations [1–7]. Therefore, the study of the failure characteristics of rocks with original crack, such as the crack propagation mechanism [8–11], mechanical properties [12–14], and acoustic emission (AE) characteristics [15–17], has been popular in recent years. Water, as a common liquid in the earth crust, is commonly present in rock flaws in underground engineering structures [18]. Due to the low permeability, rocks are often subjected to the influence of crack water pressure. In general, there are two common types of crack water pressure in rocks, as demonstrated by cases I and II in Figure 1. In case I, the crack water is not connected to a large water source, and the crack water pressure is not replenished in time during crack expansion. Therefore, the crack water pressure decreases as the crack expands. In case II, the crack water is connected to a large water source, the crack water pressure is immediately replenished during the crack propagation, so that the water pressure remains almost constant. This type of crack water pressure is termed the constant crack water pressure. With the rapid development of various types of rock engineering, increasing underground projects are being constructed under large water sources (e.g., tunneling under lakes and seabed mining). The case where constant crack water pressure is encountered is also increasing.

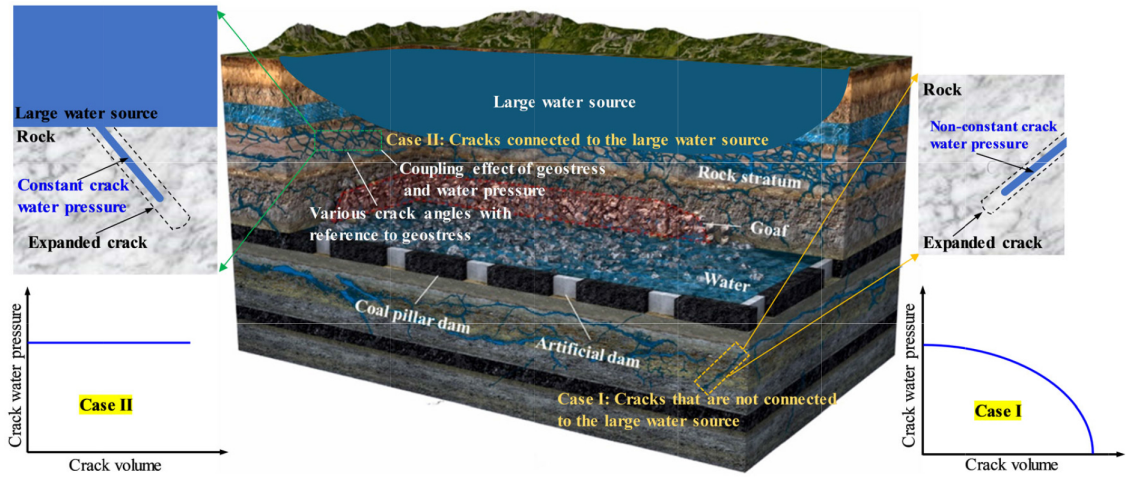

FIGURE 1: Potential cases of cracked engineering rock under hydromechanical coupling conditions with constant crack water pressure (case II) and nonconstant crack water pressure (case I; modified from Wang et al. [58]).

Therefore, it is necessary to study the effect of constant crack water pressure on the failure behavior of cracked rocks.

At present, there have been extensive numerical and experimental studies on the influence of crack water pressure on rock failure properties [19–25]. Using the numerical simulation method, Pu et al. [26] investigated the influence of crack water pressure on crack propagation and rock strength and revealed the crack damage and fracture mechanisms of rocks under water pressure. Li et al. [27] investigated the failure evolution process of uniaxially compressed rock under crack water pressure using the Fast Lagrangian Analysis of Continua in the 3D numerical model. Wang et al. [28] proposed a numerical method to simulate the crack propagation under seepage stress coupling using the extended finite element method. Li et al. [29] proposed a modeling method for rock heterogeneities and multiple hydraulic fractures propagation based on the homogenization approach and level set method. Ma et al. [30] analyzed the influence of thermophysical parameters of fracturing fluid on the damage of hot dry rocks through numerical and analytical methods. Haeri et al. [31] used the Fracture Analysis Code to simulate the effect of joint distributions in rocks on circular hole hydraulic fracturing. Through experimental methods, Gu et al. [32–34] investigated the effect of porosity on the dynamic response of water-saturated sandstone and coal. They found the weakening degree of the water-saturated sandstone and coal was positively correlated with porosity. They also explored the mechanism of porosity and water content on the fracture extension and dynamic strength of soft coal. Li et al. [35] studied the influence law of crack angle and crack water pressure on the initiation stress of cracks and breaking strength of the specimen under uniaxial compression (UC) through a transparent resin-like rock material. Fu et al. [36] described the secondary crack pattern and fracture extension process of the specimens under uniaxial and biaxial compression conditions and compared the similarities and differences in specimen fracture patterns during fracture with and without crack water pressure. Mei et al. [37] studied the effect of crack water pressure on the sprouting and expansion patterns of the prefabricated three-dimensional hollow double cracks by means of transparent resin-like rock materials. Cao et al. [38] studied the effect of crack group inclination and spacing on the crack initiation stress and peak strength of the specimens with parallel double cracks group by means of transparent resin-like rock materials. Guo et al. [39] studied the mechanical properties and failure modes of rock specimens containing three-dimensional cracks in cement mortar under anhydrous and hydraulically coupled conditions, analyzed the effects of water pressure and crack inclination, and revealed the dominant frequency characteristics of AE signals with the fracture state of the rock mass. Wei et al. [40] conducted the uniaxial and biaxial compression tests on cement mortar material under crack water pressure and analyzed in detail the crack propagation and penetration laws inside the specimens. Zhao et al. [41, 42] conducted the triaxial compression test on a single-cracked cylindrical high-strength gypsum specimen under different crack water pressures, analyzed the development types of cracks and mechanical properties, and revealed the failure laws of fractured rock masses under the combined action of water and stress. Yang et al. [43] and Mei et al. [44, 45] presented the long-term stability and strength characteristics of precracked rock specimens under hydraulic-mechanical coupling. Lin et al. [46] conducted the UC test on sandstone specimens with different crack angles under crack water pressure. They found that tensile failure mainly occurred in specimens with a crack angle from 0° to 30°, shear failure mainly occurred in specimens with a crack angle varying from 30° to 60°, and mixed tensile and shear failure mainly occurred in specimens with a crack angle from 60° to 75°. Zhao et al. [47] conducted the conventional triaxial test on limestone with single cracks of different angles under various crack water pressures. Based on the test results, they proposed a compression shear fracture criterion for the limestone with a single

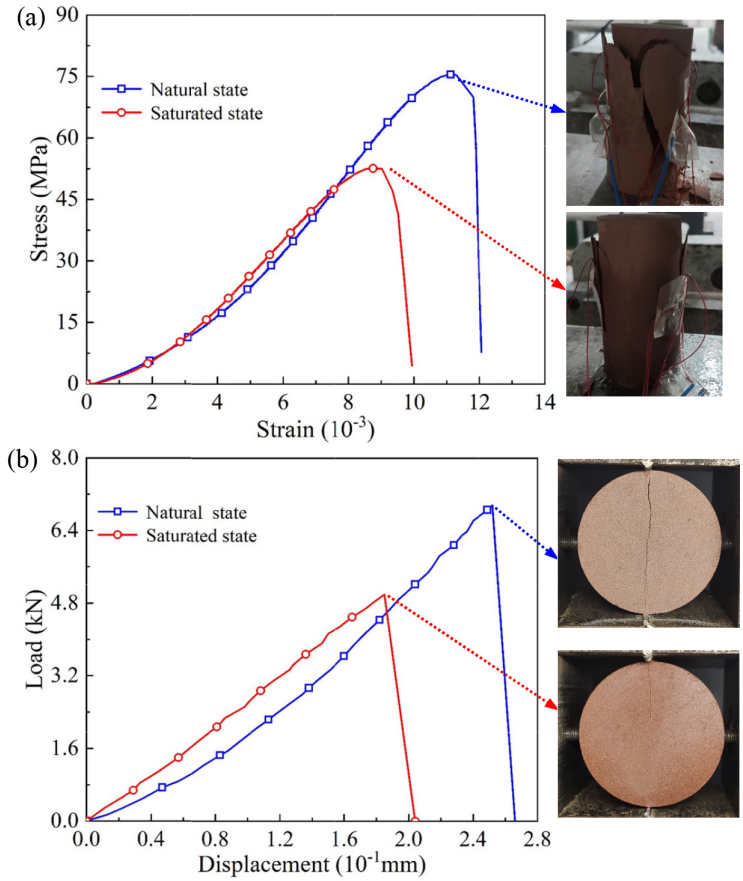

FIGURE 2: The stress-strain curves (or load-displacement curves) and failure modes of the natural and saturated red sandstone in the two types of tests. (a) UC test. (b) Brazilian splitting test.

crack under hydraulic-mechanical coupling. These existing studies have greatly contributed to the understanding of rock failure properties under hydromechanical coupling. However, most of these existing studies focused on the failure behavior of rock under nonconstant crack water pressure (case I in Figure 1), and the failure behavior of precracked rock under constant crack water pressure (case II in Figure 1) has been rarely investigated.

In this study, a device that can realize the constant crack water pressure during compression tests was introduced. The crack propagation characteristics in precracked red sandstone specimens under different constant crack water pressures were studied, and their failure characteristics were analyzed using the AE technique. In addition, the implications for support of related engineering structures were also discussed. This study provides theoretical guidance for the stability analysis of underground rock structures under large water sources.

2. Test Material

2.1. Material Characteristics. As a typical sedimentary rock, red sandstone is formed by weathering, denudation, and transportation of the source rocks over long periods in the basin [48], which is also a rock material commonly used in rock mechanics tests [49, 50]. Therefore, red sandstone was selected for the tests. The red sandstone is mined from Shandong Province, China. It presents a uniform texture, and no apparent structural surface occurs. To obtain the basic mechanical parameters of the red sandstone in the natural and saturated states, cylindrical specimens with two sizes (Φ 50 × 100 and Φ 50 × 50 mm) in both natural and saturated states were prepared for the UC test and Brazilian splitting test, respectively. The stress-strain curves (or load-displacement curves) and failure modes of the natural and saturated red sandstone specimens in UC and Brazilian splitting tests are shown in Figure 2. Under UC conditions, large and visible macroscopic cracks occurred on the surface of the natural red sandstone specimens and a large number of rock fragments fell onto the test platform. However, only visible macroscopic cracks were observed on the surface of the saturated specimens, with a small amount of rock fragments falling down the test platform. In the Brazilian splitting test, only one macroscopic crack was generated in the center of the natural and saturated red sandstone specimens. The physical and mechanical parameters of the red sandstone in natural and saturated states are illustrated in Figure 3. Compared with those of the natural red sandstone, the density of the saturated red sandstone is increased by 2.66%, and the UC strength, tensile strength, elastic modulus, and Poisson's ratio are decreased by 30.36%, 22.10%, 11.12%,

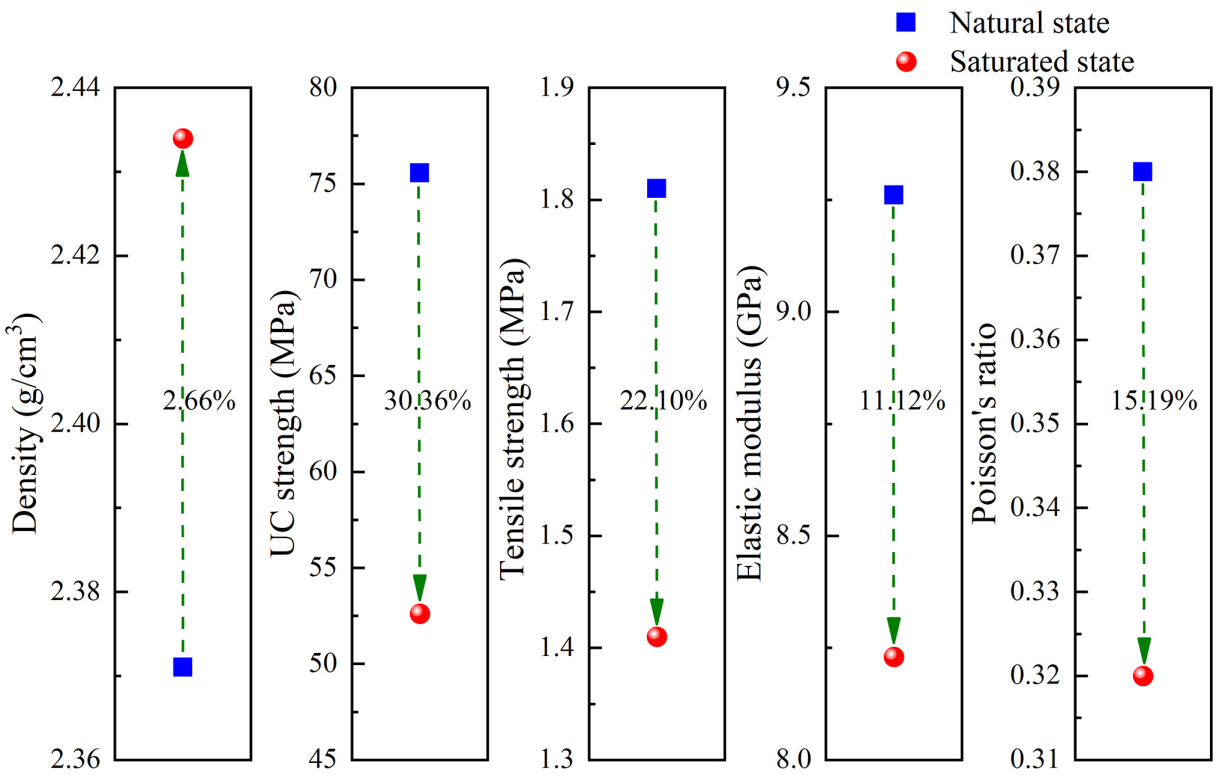

Figure 3: Basic physical and mechanical parameters of the red sandstone in natural and saturated states.

Table 1: Dimensions and test parameters of the tested specimens.

Specimen ID	Crack angle (°)	Crack size (mm)	Specimen size (mm)	Constant crack water pressure (MPa)
R0-0	0	15 × 1.5	99.9 × 35.2 × 150.3	0
R0-15	15	15 × 1.8	100.2 × 34.5 × 150.0	0
R0-45	45	15 × 1.8	99.9 × 33.9 × 150.4	0
R0-60	60	14 × 1.5	100.4 × 35.4 × 150.4	0
R0-90	90	14.3 × 1.5	100.2 × 35.4 × 150.0	0
R0.5-0	0	15 × 1.5	99.9 × 35.5 × 150.3	0.5
R0.5-15	15	15 × 1.8	100.7 × 35.3 × 150.3	0.5
R0.5-45	45	15 × 1.7	100.0 × 35.3 × 150.4	0.5
R0.5-60	60	14.5 × 1.5	100.8 × 34.9 × 150.0	0.5
R0.5-90	90	14.7 × 1.5	100.2 × 35.3 × 150.1	0.5
R1-0	0	15 × 1.5	100.4 × 35.0 × 150.3	1
R1-15	15	15 × 1.8	100.5 × 35.5 × 150.4	1
R1-45	45	14.5 × 1.6	100.3 × 35.0 × 150.3	1
R1-60	60	14.5 × 1.5	100.0 × 35.2 × 150.0	1
R1-90	90	14.4 × 1.5	100.4 × 34.9 × 150.3	1

Note: In the specimen ID, "*R*" means the "red sandstone," the first digits "0, 0.5, and 1" represent the value of the applied constant crack water pressure, and the second digits "0, 15, 45, 60, and 90" denote the precrack angle of the specimen. For example, specimen R0–0 means that a red sandstone specimen with a precrack angle of 0° was tested under the constant crack water pressure of 0 MPa.

and 15.19%, respectively. These results indicate that the mechanical parameters of the red sandstone decrease in varying degrees under water influence, and the UC strength is the most significantly weakened by water.

2.2. Specimen Preparation. The red sandstone was processed into prismatic specimens with sizes of 100 × 150 × 35 mm (width × high × thick). In Figure 4, a 15-mm-long and 1.5-mm-wide crack was prefabricated in each specimen, which penetrates the front and rear faces of the specimen. The precracked specimens were prepared with five crack angles, namely the 0°, 15°, 45°, 60°, and 90°. The ends of the specimens were polished to ensure that the flatness was controlled to within ±0.05 mm. The specific sizes of each specimen as well as the applied constant crack water pressure are shown in Table 1. The steps to prepare the saturated specimens were as follows: The specimens in the natural state were placed in a container and immersed in water. These specimens were taken out per 24 hours and weighed. When the mass of the immersed specimens remains unchanged for three consecutive times, the specimens are considered to be saturated.

3. Test System and Procedures

3.1. Principle Achieving Constant Crack Water Pressure. To achieve constant water pressure during crack propagation in the precracked specimens under compression, a device has been developed. The device consists of a pressure generation system, a pressure regulating system, a pressure stabilizing system, and a data acquisition system. It can

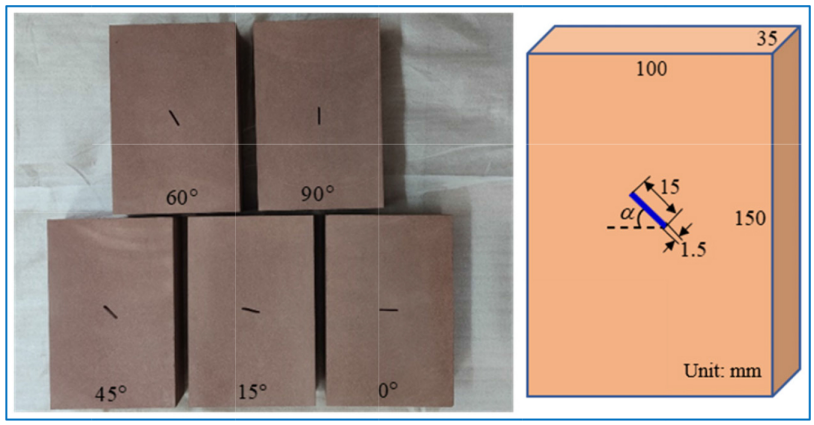

Figure 4: The precracked red sandstone specimens with different crack angles.

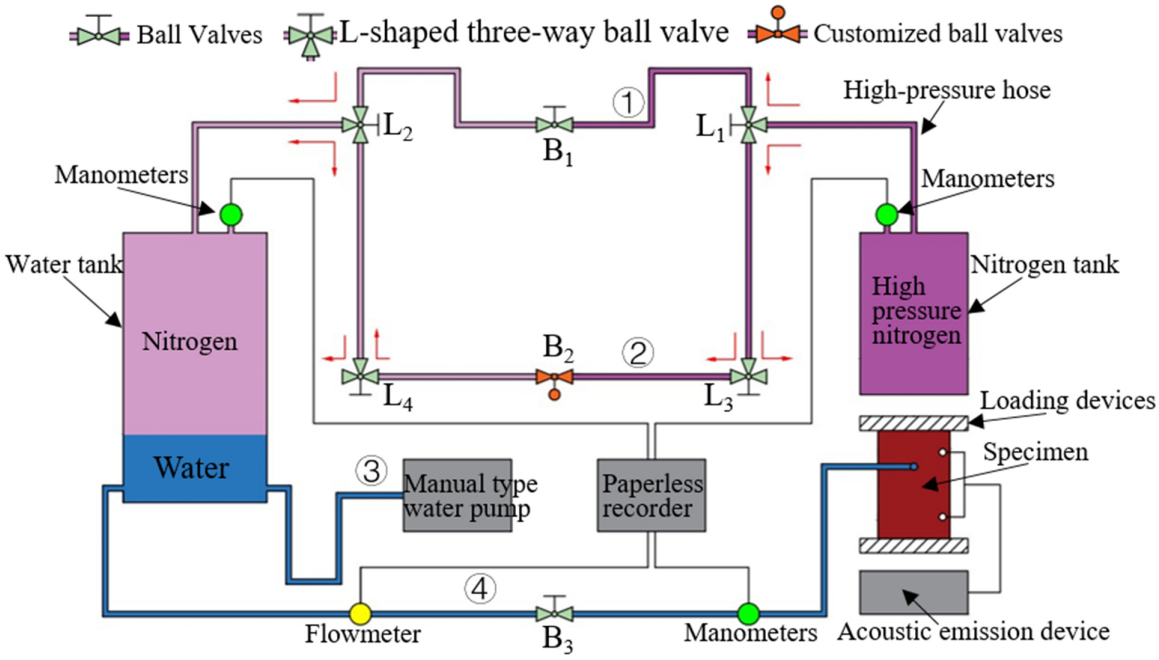

Figure 5: Working principle of the device for applying the constant crack water pressure.

apply a constant crack water pressure of up to 30 MPa. The paperless recorder can record the pressures of the nitrogen tank, the water tank, and the pipeline as well as the flow rate of the pipeline in real time. The working principle is shown in Figure 5. The compression modulus of water at room temperature is 2.15 GPa. Therefore, under smaller pressure (the highest water pressure in this test is 1 MPa), water can be regarded as incompressible. According to the Boyle's law, the product of ideal gas volume and pressure is a constant. The relationship between two gas states at the same temperature can be expressed as

$$P_A \cdot V_A = P_B \cdot V_B \quad (1)$$

where P_A and V_A are the pressure and volume of the gas before a change, and P_B and V_B are the pressure and volume of the gas after a change. Since water can be considered incompressible, the volume of crack expansion during tests can be considered to be equal to the increased volume of nitrogen in the water tank. The volume of the crack expansion is extremely small compared with that of the nitrogen in the water tank (≤0.1%). Taking the nitrogen volume increased by 0.1% as an example, its pressure reduction is less than 0.1% according to equation (1). The reduction in nitrogen pressure during crack expansion is very small. That is, the reduction of crack water pressure is very small. Therefore, it can be considered that the crack water pressure is unchanged.

3.2. Crack Water Sealing Device and Loading System. The crack water sealing device is shown in Figure 6(a). It is composed of two "Π-type" steel clamps, two polycarbonate plates, four sets of bolts and nuts, and two sealing rubber pads. Both polycarbonate plates are provided with a groove, and the sealing pad can just fit into the groove of the polycarbonate plate. One of the two polycarbonate plates contains a circular hole in the center, which is sealed and connected to a

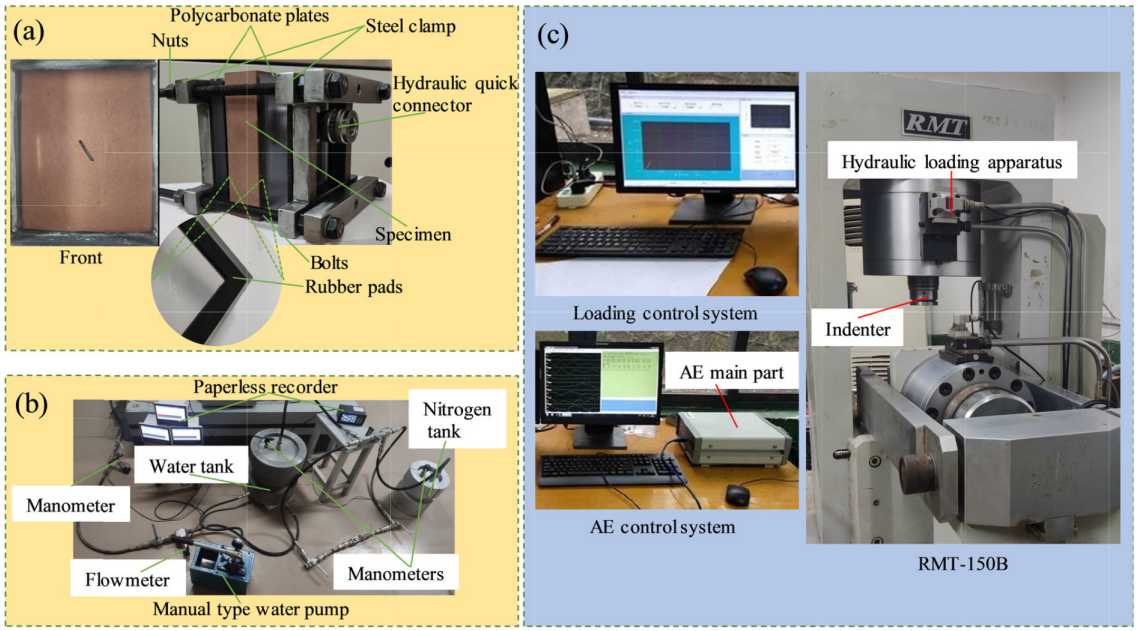

FIGURE 6: Test system used in the present work. (a) The crack water sealing device. (b) The constant crack water pressure device. (c) The loading and monitoring equipment.

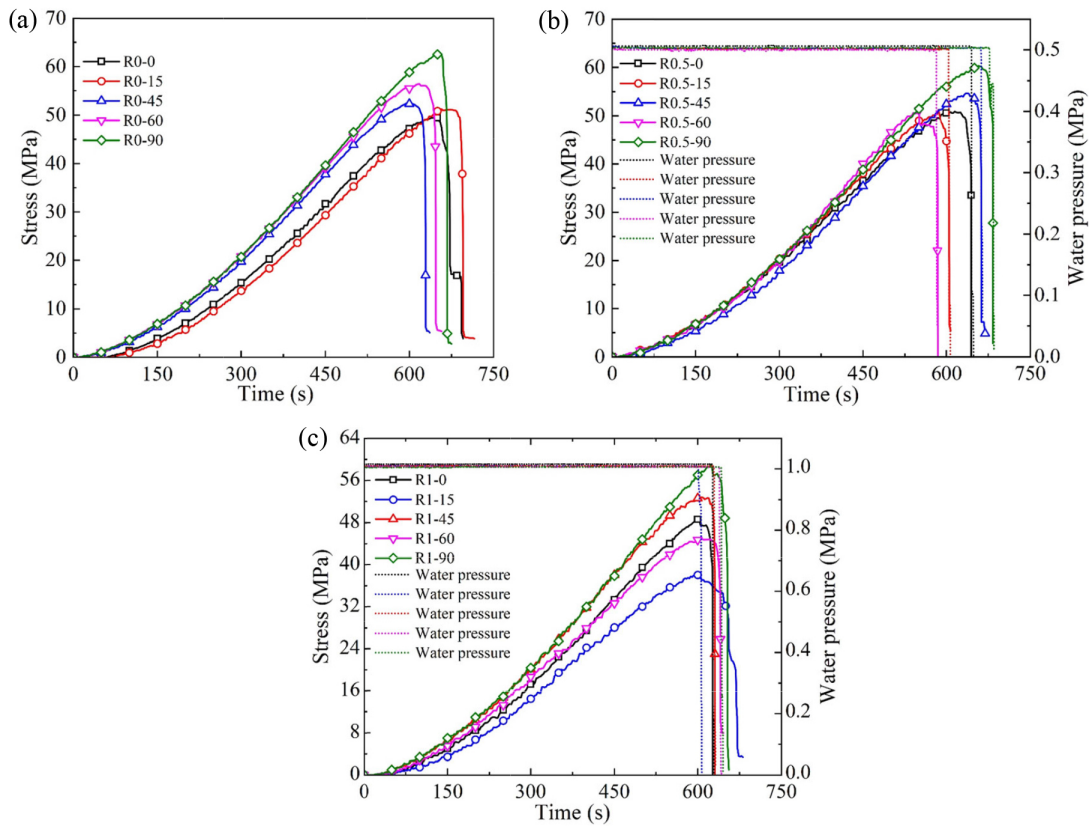

FIGURE 7: Stress history of the precracked specimens under different constant crack water pressures. (a) 0 MPa. (b) 0.5 MPa. (c) 1 MPa.

hydraulic quick connector as a high-pressure water inlet. The dimensions of the two rubber pads are the same as those of the polycarbonate plate. A torque wrench can be used to tighten the nut, and the use of an steel clamp applies the force evenly to the polycarbonate plate with a sealing rubber pads through a torque

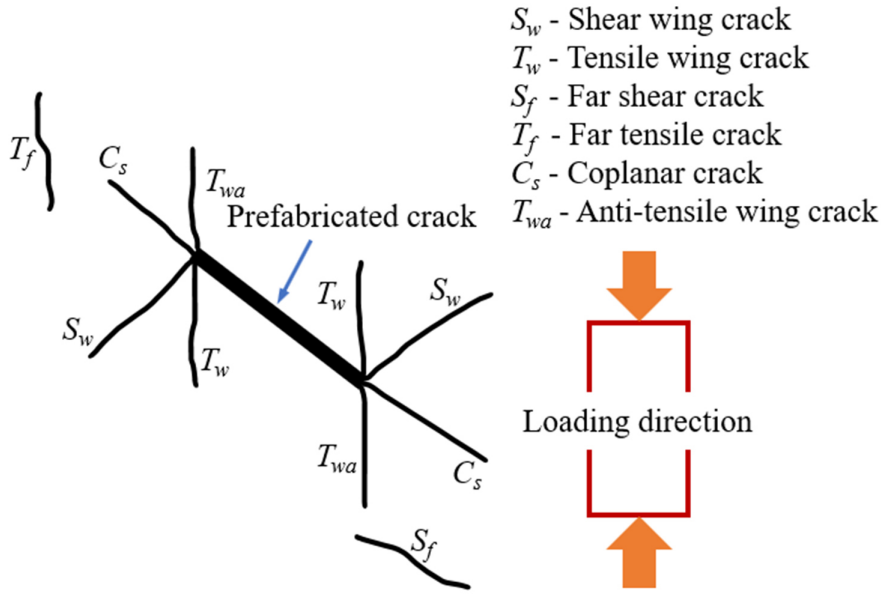

Figure 8: Crack types and nomenclature (modified from Lin et al. [55]).

wrench. This ensures that the sealing rubber pads fits tightly the to specimen and polycarbonate plate, providing a watertight seal.

Specimens were loaded using the RMT-150B rock mechanics testing machine (Figure 6(c)). The displacement control (0.002 mm/s) was adopted to compress the precracked specimens until failure. During the tests, the AE technique is used. The system trigger threshold is set to 100 mV, the preamplifier gain is 40 dB, and the sampling frequency is 3 MHz. The failure process of specimens was recorded using a high-definition camera.

3.3. Test Procedures. It was noted early that the tensile strength of the saturated red sandstone is only 1.41 MPa. Therefore, three constant crack water pressures (0, 0.5, and 1 MPa) have been set in the tests. The testing steps are as follows: (1) According to Figure 6(a), the components of the crack water sealing device and the precracked specimens were combined. Then the combination was submerged in a water tank. When the cracks of the precracked specimen and the space between the specimen surface and the polycarbonate plate were filled with water and air was discharged, the nut was tightened. (2) A specimen was installed on the test platform. The indenter of the testing machine was adhering to the upper end of the specimen with an applied force of 1 kN so that the specimen was fixed. Then, AE probes and a high-definition camera were installed. (3) A quick connector was used to connect the constant crack water pressure device to the specimen, and then constant crack water pressure was applied to the precracked specimen. (4) The specimen was compressed at a rate of 0.002 mm/s until overall failure occurred.

4. Results and Analysis

4.1. Stress History. Figure 7 shows the stress–time curves of the specimens with various crack angles under different constant crack water pressures. As shown, there is an instantaneous drop on the crack water pressure curve after the specimens reach their peak stress, exhibiting the brittle fracture characteristics of red sandstone specimens under hydromechanical coupling. During the entire loading process, the specimens experience four stress history segments: the nonlinear segment, the elastic linear segment, the rapid cracking segment, and the postpeak segment. It can also be observed that the crack water pressure remains constant during the whole prepeak loading of specimens, which further confirms the reliability of the constant crack water pressure device.

4.2. Fracture Process and Failure Modes. In previous studies, the classification of crack types has been detailed [51–54]. In this study, the crack types were identified by referring to Lin et al. [55], as shown in Figure 8.

During the loading of specimens, a high-stress concentration zone first occurs at the prefabricated crack location where the crack initiates. With further increase in the applied stress, far cracks appear. Taking the 45° precracked specimen as an example, the cracking sequence was analyzed. As shown in Figure 9, the fracture process is similar for the precracked specimens in the absence and presence of constant crack water pressure. As the applied stress increases, wing cracks are generated at the end of the

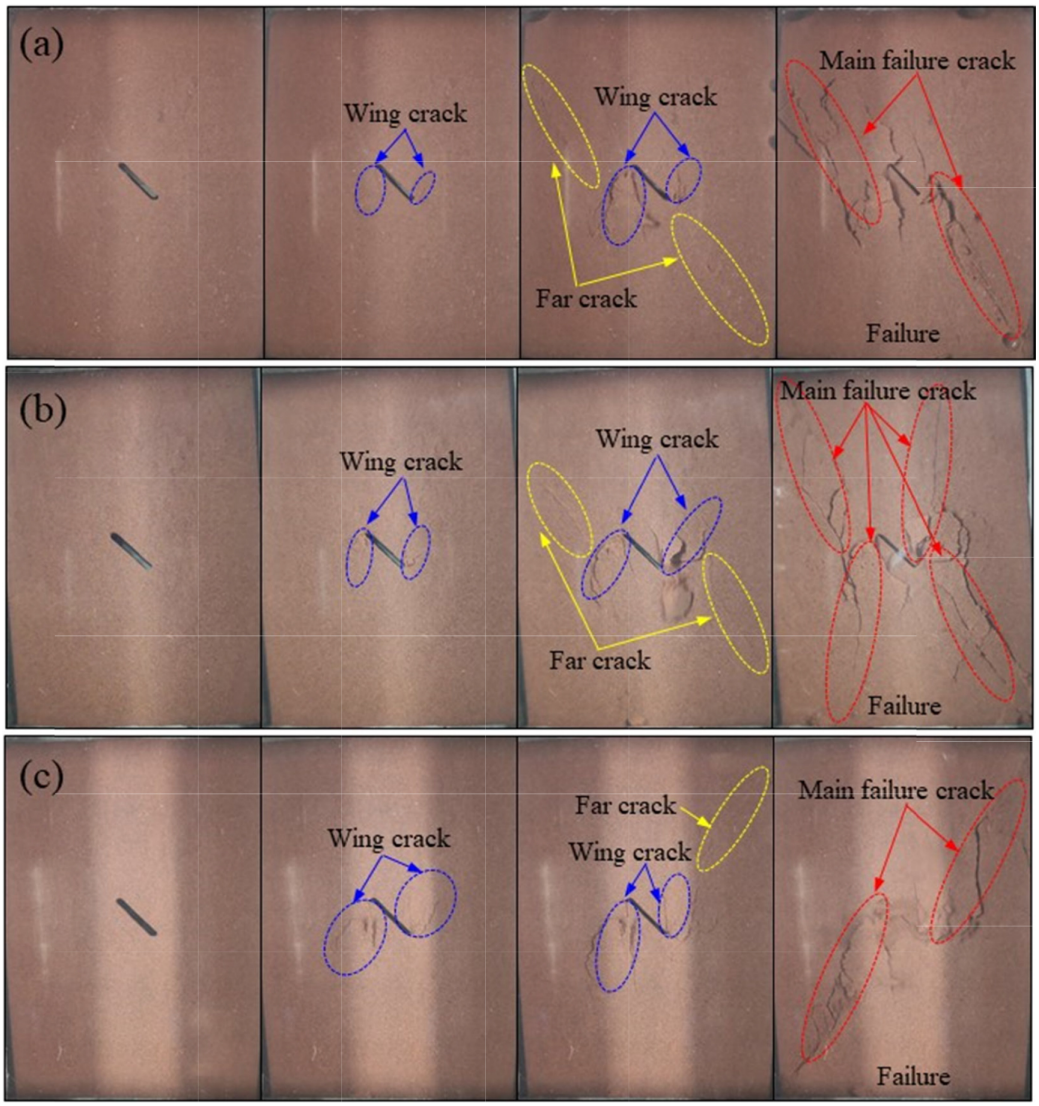

Figure 9: Representative cracking process of the specimens with 45° precrack angle under different constant crack water pressures. (a) 0 MPa. (b) 0.5 MPa. (c) 1.0 MPa.

prefabricated cracks. When the stress increases to a certain extent, far cracks begin to occur, and wing cracks develop further. The final wing cracks or far cracks further develop into the main failure crack (F_m). It is noteworthy that the direction of F_m varies as the constant crack water pressure increases (Figure 9).

To further observe the failure modes of the specimens, the surface rock fragments that are about to peel off were removed, and the main internal failure cracks were marked with red lines, as shown in Figure 10. Under the constant crack water pressure of 0 MPa, both the shear wing crack and tensile wing crack of the 0° precracked specimens were fully developed. The shear wing crack and far shear crack developed together as the F_m. Finally, the specimen showed an "X"-shaped shear failure (Figure 10(a)). From Figures 10(d), (g), and (j), compared with those in the 0° precracked specimens, shear wing crack, and tensile wing crack developed to a lesser extent in the 15°, 45°, and 60° precracked specimens. Both shear wing crack and tensile wing crack had developed only a small distance when far shear crack appeared. Finally, far shear crack developed as the F_m and intersected with the shear wing crack, and the single oblique shear failure of the specimen occurred. From Figure 10(m), no wing cracks were developed in the 90° precracked specimen. As the applied stress increased, spalling first occurred on the prefabricated crack. Then, with continuously increasing stress, far shear crack occurred. Finally, the far shear crack developed into the F_m, and the specimen shows a single oblique shear failure. It is worth noting that the F_m direction of the inclined precracked specimens (i.e., 15°, 15°, and 60° precracked specimens) is at a smaller acute angle to the direction of the prefabricated cracks. The F_m direction of the specimens with a large prefabricated crack angle is basically the same as the prefabricated crack direction (see Figures (g) and (j)).

The failure modes of specimens change dramatically when a constant crack water pressure is applied to the prefabricated cracks. When the constant crack water

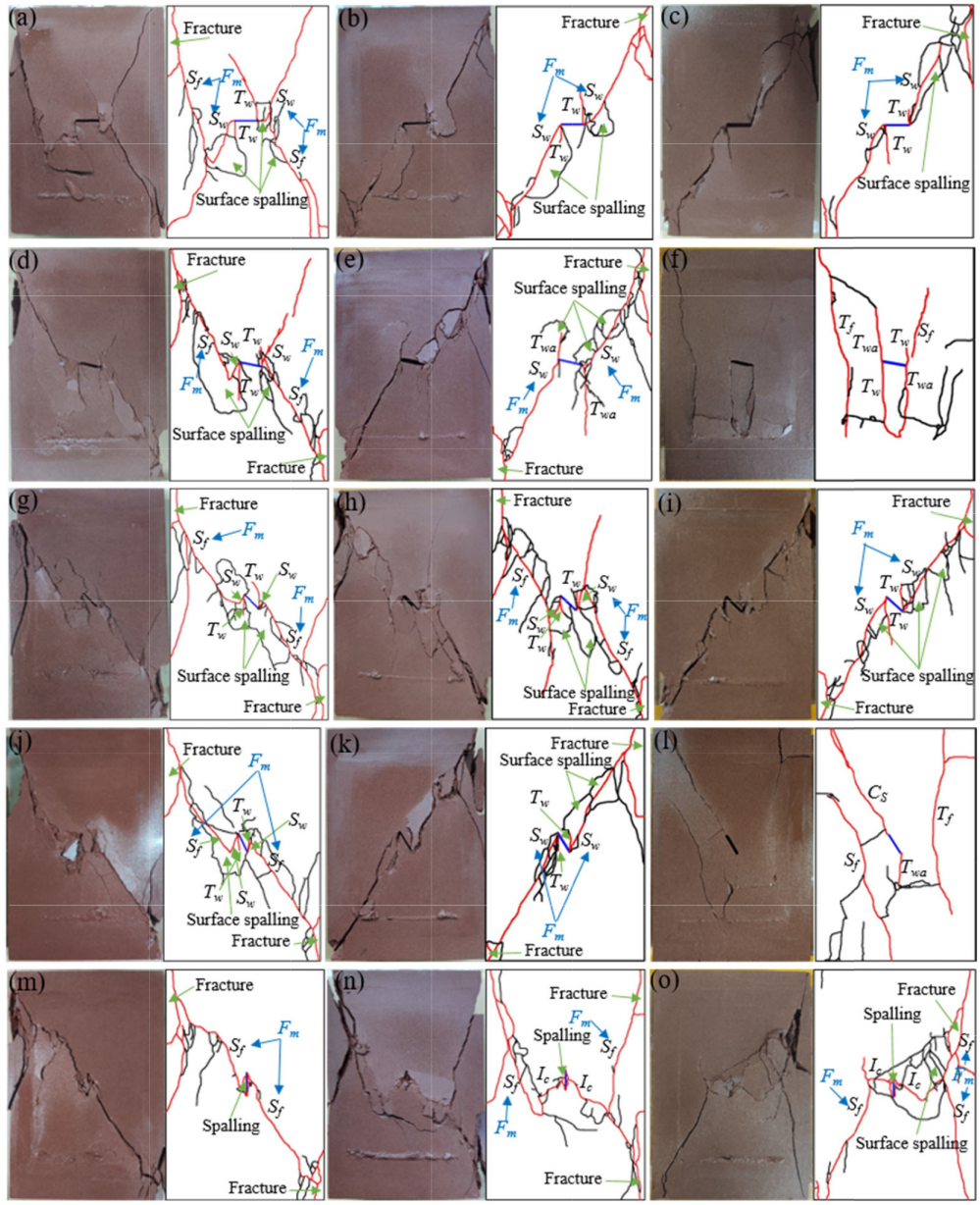

Figure 10: Failure modes of the specimens with different precrack angles under various constant water pressures. (a) R0–0. (b) R0.5–0. (c) R1–0. (d) R0–15. (e) R0.5–15. (f) R1–15. (g) R0–45. (h) R0.5–45. (i) R1–45. (j) R0–60. (k) R0.5–60. (l) R1–60. (m) R0–90. (n) R0.5–90. (o) R1–90.

pressure is 0.5 MPa, the F_m direction of 0°, 15°, and 60° precracked specimens actually transforms to be basically the same as the direction of shear wing cracks, as shown in Figure 10(b), (e), and (k) . A single oblique shear failure of the specimen occurred. This indicates that the presence of constant crack water pressure promotes the development of shear wing cracks, causing the specimen to fail along the direction of shear wing cracks. The F_m direction of the 45° precracked specimen does not coincide with that of the shear wing cracks (Figure 10(h)). However, due to the promotion effect of constant crack water pressure, shear wing cracks were developed to a larger extent, and finally, the specimen showed an "X"-shaped shear failure. This is attributed to the insufficient promotion effect of low constant crack water pressure (0.5 MPa) on shear wing cracks. However, under the constant crack water pressure of 1 MPa, the F_m direction transformation of 45° precracked specimens is basically the same as that of the shear wing cracks (see Figure 10(i)). This indicates that the constant crack water pressure weakly promotes the shear wing cracks in the 45° precracked specimens. When the constant crack water pressure is 1 MPa, the failure mode of the 0° precracked specimen is basically the same as that under the constant crack water pressure of 0.5 MPa (see Figures 10(b) and (c)). With the constant crack water pressure of 1 MPa, the tensile wing crack and antitensile wing crack of the 15° precracked specimen were developed to a larger extent (Figure 10(f)). The final

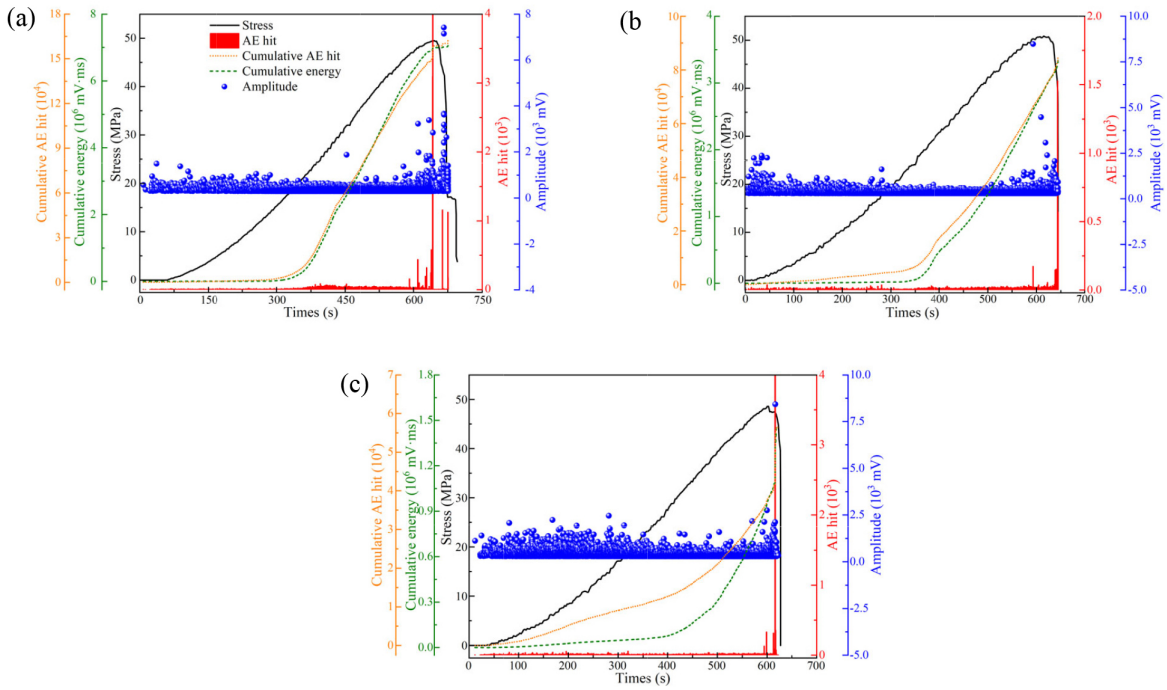

Figure 11: Stress and AE characteristics of 0° precracked specimens under different constant crack water pressures. (a) R0–0. (b) R0.5–0. (c) R1–0.

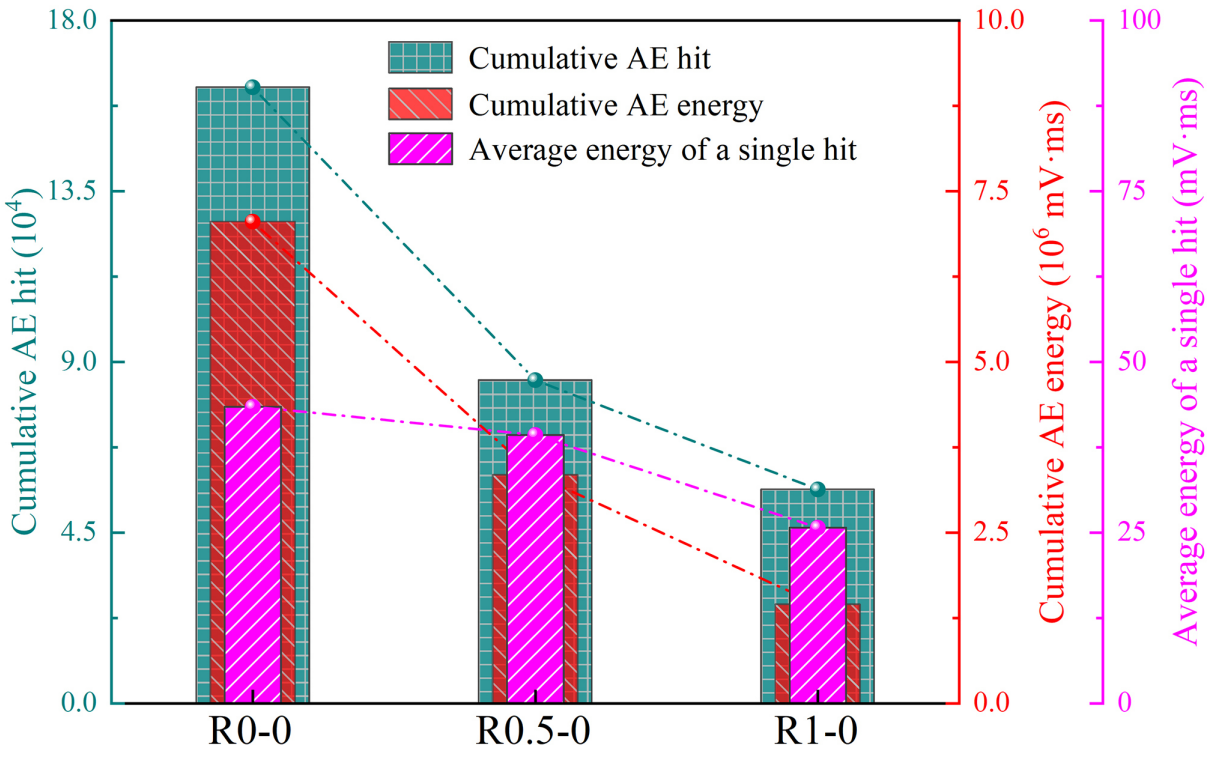

Figure 12: Typical cumulative AE hits, cumulative AE energy, and average energy during a single hit.

specimen showed a more complex mixed tensile-shear failure. This indicates that the presence of constant crack water pressure can also significantly promote the propagation of tensile wing crack and antitensile wing crack. When the constant crack water pressure is 1 MPa, a coplanar crack occurred along the prefabricated crack in the 60° precracked specimen under axial loading (see Figure 10(l)). The coplanar crack generally appeared during hydraulic splitting. It indicates that when the constant crack water pressure reaches a certain degree, the existence of axial

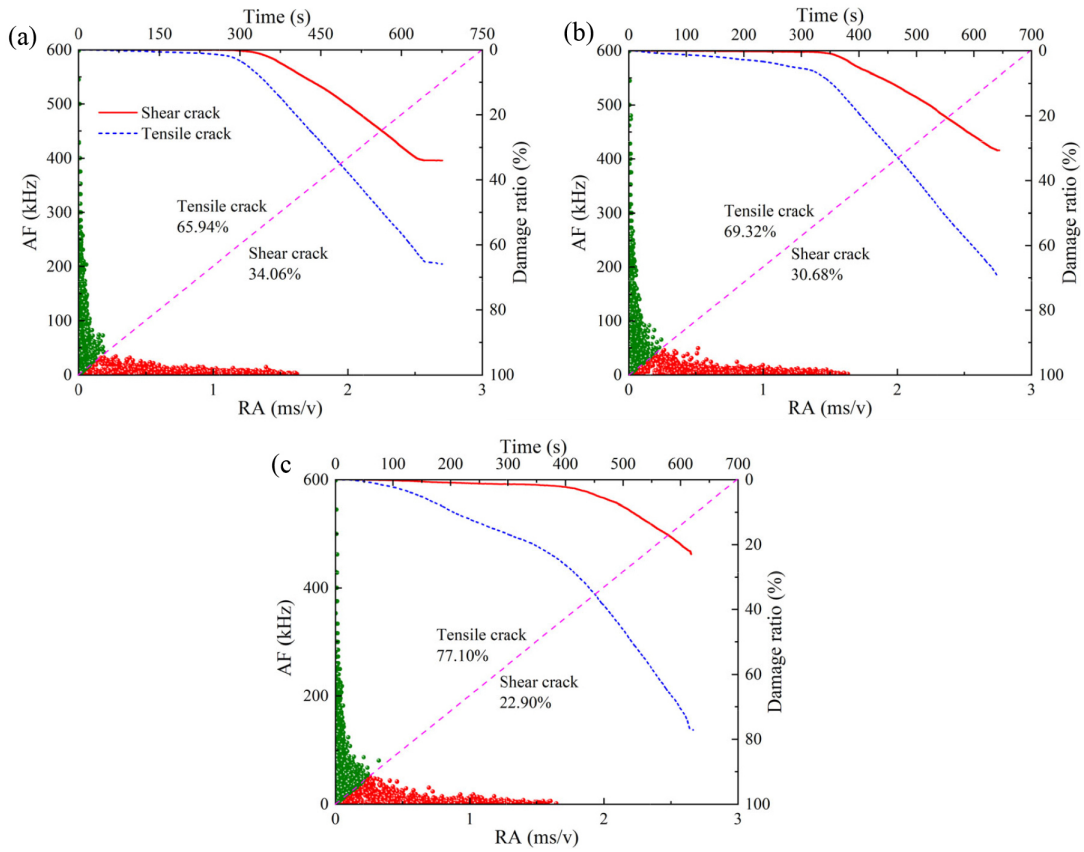

Figure 13: Typical RA-AF relations and crack percentage of the tested specimens. (a) R0–0. (b) R0.5–0. (c) R1–0.

stress causes a hydraulic splitting effect on the specimen and also suggests that the fracture behavior of 60° precracked specimen is more sensitive to the constant crack water pressure. For the 90° precracked specimens, the presence of constant crack water pressure promotes the development of irregular cracks at the prefabricated crack after spalling (see Figures 10(n) and 10(o)). When the applied stress increases to a certain level, far shear crack appears, and the specimen finally fails in a more complex shear mode. The complex failure mode may be related to the irregular shape of the prefabricated cracks after spalling. The spalling effect of the prefabricated crack wall resulted in more complex irregular cracks, which ultimately led to the complexity of the failure mode of the specimen.

When the constant crack water pressure is 0 MPa, the longest wing crack is observed for the 0° precracked specimen, followed by that of the 15° precracked specimen, and the wing cracks are shorter in the 45° and 60° precracked specimens. A spalling occurs in prefabricated crack walls of 90° precracked specimens, but no wing crack develops. The F_m direction of the inclined precracked specimen (the precrack angles are 15°, 45°, and 60°) is at a small acute angle to the direction of the prefabricated crack. The constant crack water pressure has a significant promotion effect on the propagation of wing cracks (especially for the shear wing crack). The promotion effect is influenced by the precrack angle and water pressure. When the constant crack water pressure is 0.5 MPa, the F_m direction of the 0°, 15°, and 60° precracked specimens is the same as that of the shear wing crack, the shear wing crack of the 45° precracked specimen is greatly developed, and irregular cracks are produced near the prefabricated crack when the precrack angle is 90°. When the constant crack water pressure is 1 MPa, the F_m of the 0°, 15°, and 45° precracked specimens is all controlled by wing cracks, coplanar cracks appear in the 60° precracked specimens, and irregular cracks are produced in the 90° precracked specimens.

4.3. AE Characteristics. It has been reported that there is a connection between AE signals and rock deformation and failure. Therefore, in this paper, taking the 0° precracked specimens as examples, the AE characteristics of the rock specimens under different constant crack water pressures were analyzed. Figure 11 shows the AE hits, cumulative AE hits, cumulative AE energy, and amplitude of the 0° precracked specimens during compression under the constant crack water pressures of 0, 0.5, and 1.0 MPa. As shown in Figure 11, in the early loading of the specimen, the AE hits were very low, and the cumulative AE hits and cumulative AE energy were inconspicuous. This finding indicates that currently, the crack development inside the specimens is less. In the later stage of loading, the AE hits increase sharply, and the cumulative AE hits and cumulative AE energy increase significantly. High amplitudes of AE hits

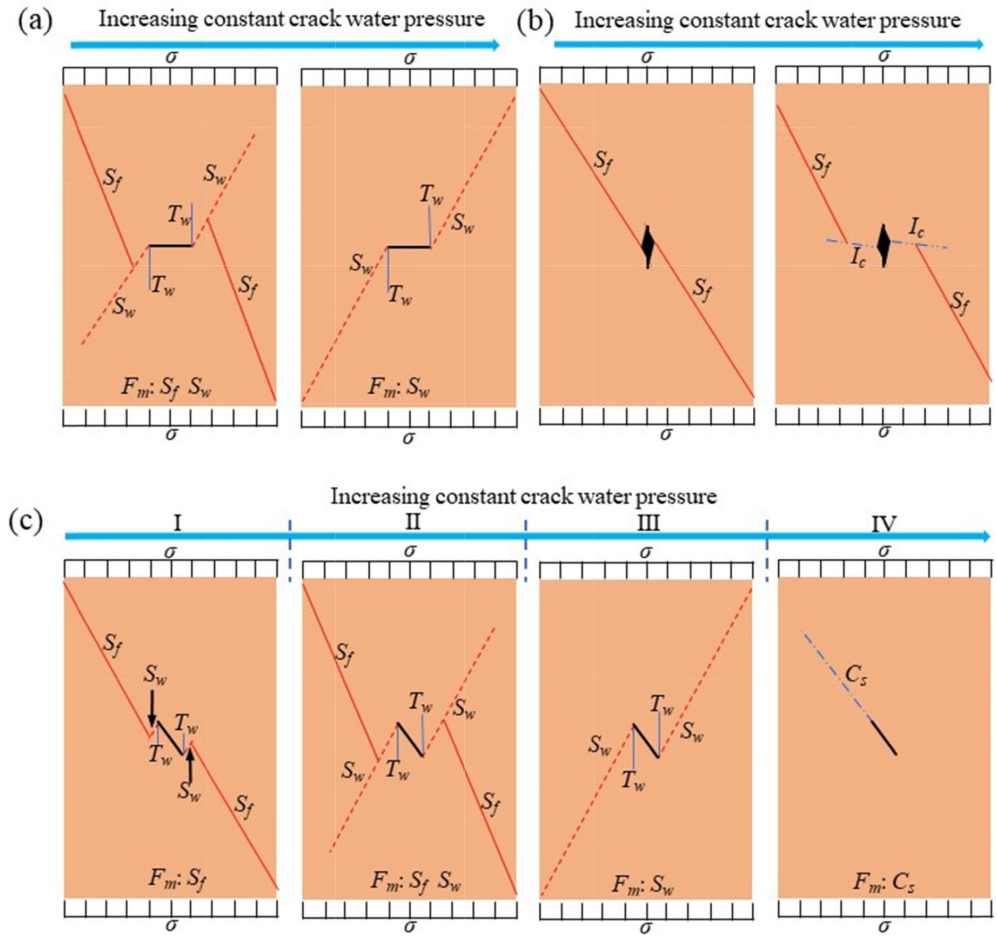

Figure 14: Sketch of failure modes of the precracked rock specimens under increasing constant crack water pressure.

mainly occur in the early loading stage and the last loading stage.

Figure 12 shows the cumulative AE energy, cumulative AE hits, and average energy during a single hit of the 0° precracked specimens under different constant crack water pressures. Under the constant crack water pressures of 0, 0.5, and 1 MPa, the cumulative AE energy during compression of the specimens reaches 7.0565 × 106, 3.3483 × 106, and 1.4515 × 106 mV·ms, respectively; and the cumulative AE hits are 162,424, 85,200, and 56,386 times, respectively. Both the cumulative AE energy and cumulative AE hits decrease with increasing constant crack water pressure. This indicates that the number of cracks generated during final specimen damage decreases with increasing constant crack water pressure. The average energy for a single AE hit under 0, 0.5, and 1 MPa constant crack water pressure is 43.45, 39.30, and 25.74 mV·ms, respectively. The average energy for a single AE hit decreases as the constant crack water pressure increases. This finding indicates that the presence of constant crack water pressure promotes crack expansion and reduces the energy required for crack expansion.

It has been reported that shear cracks can be characterized by high risetime amplitude (RA) and low average frequency (AF) values, and tensile cracks can be characterized by low RA and high AF values [56]. For brittle materials, the splitting line is taken as RA:AF = 1:200 to obtain the crack classification results [57]. Figure 13 shows the percentage of shear and tensile cracks in 0° precracked specimens during compression. As the number of cracks essentially characterizes the damage degree of the rock specimen, the damage ratio is also given as the ratio of shear or tensile cracks to the total cracks. In the early stage of loading, the development of tensile and shear cracks is not obvious under the constant crack water pressure of 0 MPa. However, the number of two crack types increases sharply around 300 seconds (Figure 13(a)). Finally, the tensile cracks and shear cracks account for 65.94% and 34.06% of the total cracks, respectively. Under the constant crack water pressure of 0.5 MPa, the development of shear cracks is not obvious during early loading. The number of tensile cracks under the constant crack water pressure of 0.5 MPa is greater than that under the constant crack water pressure of 0 MPa. At 350 seconds, the ratio of the two crack types increases dramatically. Finally, the tensile cracks and shear cracks accounted for 69.32% and 30.68% of the total cracks, respectively (Figure 13(b)). As shown in Figure 13(c), compared with the specimens under the constant crack water pressure of 0 and 0.5 MPa, the specimen

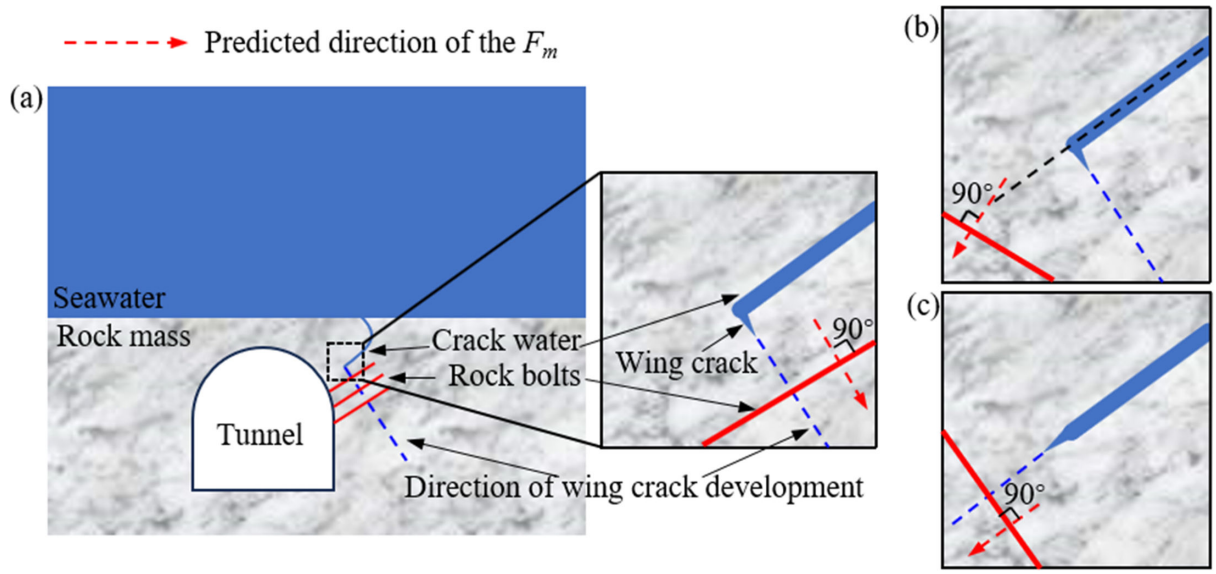

FIGURE 15: Schematic for potential design of rock bolts support. (a) F_m along the direction of the shear wing crack. (b) F_m has a small acute angle with the initial crack. (c) F_m along the direction of the initial crack.

under the constant crack water pressure of 1 MPa exhibited significantly higher development of shear and tensile cracks during early loading. The tensile cracks accounted for 20% of the total cracks at about 400 seconds. Finally, the tensile and shear cracks accounted for 77.10% and 22.90% of the total cracks, respectively. It shows that with increasing constant crack water pressure, the ratio of tensile cracks increases, and the ratio of shear cracks to total cracks decreases. The reason may be that the presence of constant crack water pressure reduces the friction between fracture surfaces, resulting in a decrease in the ratio of shear cracks.

5. Discussion

A prediction of potential rock failure modes is significant to ensure effective reinforcement of underground rock structures. As mentioned earlier, it is evident that the presence of constant crack water pressure significantly influences the cracking behaviors. Figure 14 illustrates the variations in the failure mode of the rock specimens with different precrack angles under increasing constant crack water pressure. The F_m directions of precracked rock at different crack dips were presented. From Figure 15, rock bolts can be installed perpendicular to the predicted F_m direction to reinforce the rock structure. This approach allows a prediction of the F_m direction and an implementation of reinforcement measures in the vertical direction to enhance the stability and safety of engineering rock structures under large water source such as seabed.

When the initial crack angle is 0°, under no or small constant crack water pressure, the F_m develops along the shear wing crack direction and the direction of far shear crack with large obtuse angles to the shear wing crack, as shown in Figure 14(a). In this scenario, reinforcement measures should be executed in both directions. When the constant crack water pressure reaches a certain level, the F_m mainly propagates along the shear wing crack direction (see Figure 14(a), right). In this case, the reinforcement can be designed considering the direction of the generated shear wing crack, as illustrated in Figure 15(a). For rock masses with an initial crack angle of 90°, with no or low constant crack water pressure, rock masses often exhibit oblique shear failure under stress (see Figure 14(b)). Under a given constant crack water pressure, irregular cracks are created near the initial cracks that have spalled under the action of constant crack water pressure. However, due to the irregularity of the cracking process, a more complex failure mode occurs, making it challenging to predict the direction of F_m (see Figure 14(b)).

When the initial crack is inclined (see Figure 14(c)), under increasing constant crack water pressure, the evolution of F_m can be categorized into four distinct phases. During the initial phase (i.e., Phase I), the direction of F_m in the rock mass is at an acute angle to the initial crack direction under relatively low constant crack water pressure. When the initial crack angle is larger, the F_m direction can be considered to be basically the same as the initial crack direction. At this juncture, the failure mode of rock mass is governed by the physical attributes of the initial crack, including the length and angle. Consequently, reinforcement strategies can be devised based on Figure 15(b). In the second phase (Phase II), the failure mode of the rock mass is controlled by a combination of the initial crack and the shear wing crack, which can be reinforced according to Figures 15(a) and 15(b). In the third phase (Phase III), the failure mode of the rock mass is mainly controlled by the presence and growth of shear wing crack, and the rock structure can be reinforced according to Figure 15(a). In the fourth phase (Phase IV), the locations of the initial cracks become susceptible to the formation

of coplanar cracks, and the reinforcement measures can be devised based on Figure 15(c). These distinct phases delineate the effect of constant crack water pressure on the evolution direction of F_m within rock mass, and the related reinforcement measures using rock bolts are presented.

6. Conclusions

(1) With no constant crack water pressure, the longest wing crack is observed for the 0° precracked specimen, followed by that of the 15° precracked specimen, and the wing cracks are shorter in the 45° and 60° precracked specimens. The collapse occurs in prefabricated crack walls of 90° precracked specimens, but no wing crack develops. The direction of the main failure crack in the inclined precracked specimens is at a small acute angle to the direction of the prefabricated crack.

(2) The presence of constant crack water pressure has a significant promotion effect on the development of wing cracks, especially for the shear wing crack. The promotion effect is influenced by the precrack angle and water pressure. As the constant crack water pressure increases, the failure mode of the 0° precrack specimen changes from "X"-shear failure to the single oblique shear failure along the shear wing crack direction, the main failure crack of the inclined precracked specimens (precrack angles of 15°, 45°, and 60°) changes from a small acute angle with the prefabricated crack to a direction along the shear wing crack, and irregular cracks occur at the chipped prefabricated crack in the 90° precracked specimen.

(3) The average energy for a single hit, cumulative AE energy, and cumulative AE hits decrease with the increasing constant crack water pressure. The presence of constant crack water pressure promotes crack expansion and reduces the energy required for crack expansion. The number of cracks produced during specimen failure decreases as the constant crack water pressure increases. The proportion of the tensile cracks increases and that of the shear cracks decreases with the increasing constant crack water pressure.

Data Availability

All data that support the findings of this study are included within the article.

Conflicts of Interest

The authors declare that they have no conflict of interest.

Acknowledgments

This work was supported by the National Natural Science Foundation of China (52104133 and 52304227), the Natural Science Foundation of Hunan Province (2021JJ40465 and 2023JJ40548), the Henan Postdoctoral Foundation (HN2022015), and the Research Project of Education Department of Hunan Province (20C1623 and 22B0426).

References

[1] H. L. Le, J. H. Wei, S. R. Sun, and Y. Lv, "Experimental investigation on strength and crack mechanism of rock-like samples with open-closed cross-flaws under uniaxial compression," *Lithosphere*, vol. 2022, no. special 10, p. 9681138, 2022.

[2] T. Zhou, J. R. Chen, H. P. Xie, C. T. Zhou, F. Wang, and J. B. Zhu, "Failure and mechanical behaviors of sandstone containing a pre-existing flaw under compressive–shear loads: insight from a Digital Image Correlation (DIC) analysis," *Rock Mechanics and Rock Engineering*, vol. 55, no. 7, pp. 4237–4256, 2022.

[3] Y. M. Wang, Y. Q. Wang, S. Luo, H. Liu, G. S. Yi, and K. Peng, "Influence of the crack angle on the deformation and failure characteristics of sandstone under stepped cyclic uniaxial compression with a constant lower limit," *Mathematics*, vol. 11, no. 9, p. 2187, 2023.

[4] P. L. Zhang, F. Q. Gong, S. Luo, X. F. Si, and L. Xu, "Damage Constitutive model of uniaxially compressed coal material considering energy dissipation," *Journal of Materials Research and Technology*, vol. 27, pp. 920–931, 2023.

[5] X. F. Si, S. Luo, and Y. Luo, "A review of mechanical properties and rockburst investigation of transversely isotropic rocks by experimental technique," *Materials*, vol. 16, no. 8, p. 3183, 2023.

[6] X. F. Si, Y. Luo, F. Q. Gong, J. C. Huang, and K. F. Han, "Temperature effect of rockburst in granite caverns: insights from reduced-scale model true-triaxial test," *Geomechanics and Geophysics for Geo-Energy and Geo-Resources*, vol. 10, p. 26, 2024.

[7] K. Peng, J. Ren, Y. M. Wang, S. Luo, and K. Long, "Mechanical and damage evolution characteristics of granite after heating-cooling cycles," *Journal of Central South University*, vol. 30, pp. 4082–4096, 2023.

[8] H. Haeri, "Propagation mechanism of neighboring cracks in rock-like cylindrical specimens under uniaxial compression," *Journal of Mining Science*, vol. 51, no. 3, pp. 487–496, 2015.

[9] H. Haeri, "Simulating the crack propagation mechanism of pre-cracked concrete specimens under shear loading conditions," *Strength of Materials*, vol. 47, no. 4, pp. 618–632, 2015.

[10] H. Haeri, V. Sarfarazi, M. Yazdani, A. B. Shemirani, and A. Hedayat, "Experimental and numerical investigation of the center-cracked Horseshoe disk method for determining the mode I fracture toughness of rock-like material," *Rock Mechanics and Rock Engineering*, vol. 51, no. 1, pp. 173–185, 2018.

[11] Y. Zhang, G. Q. Chen, Y. H. Gao, Y. T. Xu, and D. Liu, "Mechanical behavior and failure process of hard rock with rock bridge under Uniaxial compression test," *Lithosphere*, vol. 2022, no. Special 11, p. 1492868, 2022.

[12] X. F. Si, X. B. Li, F. Q. Gong, L. Q. Huang, and C. D. Ma, "Experimental investigation on Rockburst process and characteristics of a circular opening in layered rock under three-dimensional stress conditions," *Tunnelling and Underground Space Technology*, vol. 127, p. 104603, 2022.

[13] X. F. Si, Y. Luo, and S. Luo, "Influence of Lithology and bedding orientation on failure behavior of "D" shaped tunnel," *Theoretical and Applied Fracture Mechanics*, vol. 129, p. 104219, 2024.

[14] P. Guo, G. D. Li, F. Luo, and X. J. Tang, "Influence of the preexisting fracture network on the mechanical properties of rock mass and the secondary crack propagation," *Geofluids*, vol. 2022, p. 9603766, 2022.

[15] J. W. Fu, T. Li, and H. Haeri, "Acoustic emission monitoring of crack growth from echelon notches using numerical simulation," *Strength of Materials*, vol. 55, no. 1, pp. 128–145, 2023.

[16] Y. Y. Wang, H. C. Deng, Y. Deng, K. P. Chen, and J. H. He, "Study on crack dynamic evolution and damage-fracture mechanism of rock with pre-existing cracks based on acoustic emission location," *Journal of Petroleum Science and Engineering*, vol. 201, p. 108420, 2021.

[17] W. Q. Ma, J. T. Wang, X. X. Li, and T. X. Wang, "Crack evolution and acoustic emission characteristics of rock specimens containing random joints under uniaxial compression," *Acta Geophysica*, vol. 69, no. 6, pp. 2427–2441, 2021.

[18] S. Luo, F. Q. Gong, K. Peng, and Z. X. Liu, "Influence of water on rockburst proneness of sandstone: insights from relative and absolute energy storage," *Engineering Geology*, vol. 323, p. 107172, 2023.

[19] Z. D. Zhu and D. Hu, "The effect of Intestitial water pressure on rock mass strength," *Rock and Soil Mechanics*, vol. 21, no. 1, pp. 64–67, 2000.

[20] Y. L. Zhao, P. Cao, Y. D. Wen, H. Yang, and J. T. Li, "Damage fracture failure mechanism of compressive-shear rock cracks under seepage pressure," *Journal of Central South University*, vol. 39, no. 4, pp. 838–844, 2008.

[21] Y. L. Zhao, L. M. Tang, Q. Liu, and S. L. Xie, "The micro damage model of the cracked rock considering seepage pressure," *Geotechnical and Geological Engineering*, vol. 37, no. 2, pp. 965–974, 2019.

[22] Y. L. Zhao, Q. Liu, J. Liao, Y. X. Wang, and L. M. Tang, "Theoretical and numerical models of rock wing crack subjected to hydraulic pressure and far-field stresses," *Arabian Journal of Geosciences*, vol. 13, no. 18, p. 926, 2020.

[23] X. B. Li, X. P. He, and H. J. Chen, "Crack initiation characteristics of opening-mode crack embedded in rock-like material under seepage pressure," *Chinese Journal of Rock Mechanics and Engineering*, vol. 31, no. 7, pp. 1317–1324, 2012.

[24] F. Cappa, Y. Guglielmi, P. Fénart, V. Merrien-Soukatchoff, and A. Thoraval, "Hydromechanical interactions in a fractured carbonate reservoir inferred from hydraulic and mechanical measurements," *International Journal of Rock Mechanics and Mining Sciences*, vol. 42, no. 2, pp. 287–306, 2005.

[25] H. Y. Liu, Y. Z. Zhou, G. X. Zhang, L. Xue, and X. H. Zheng, "Compression-shear initiation criterion for rockmass crack under water pressure," *Journal of Central South University*, vol. 54, no. 3, pp. 920–929, 2023.

[26] C. Z. Pu, P. Cao, C. Y. Zhang, and Z. Z. Fu, "Fracture failure mechanism of rock with closed crack and judging criterion of seepage pressure under biaxial compression," *Rock and Soil Mechanics*, vol. 36, no. 1, pp. 56–60, 2015.

[27] Y. Li, H. Zhou, W. S. Zhu, S. C. Li, and J. Liu, "Numerical study on crack propagation in brittle jointed rock mass influenced by fracture water pressure," *Materials*, vol. 8, no. 6, pp. 3364–3376, 2015.

[28] C. Wang and Q. Y. Zhang, "Study of the crack propagation model under seepage–stress coupling based on XFEM," *Geotechnical and Geological Engineering*, vol. 35, no. 5, pp. 2433–2444, 2017.

[29] M. Li, P. J. Guo, D. Stolle, and S. Y. Liu, "Modeling method for rock heterogeneities and multiple hydraulic fractures propagation based on homogenization approach and PHF-LSM," *Geomechanics for Energy and the Environment*, vol. 33, p. 100442, 2023.

[30] W. W. Ma, C. Yang, S. F. Ahmed, et al., "Effects of thermo-physical parameters of fracturing fluid on hot dry rock damage in hydraulic fracturing," *Geomechanics for Energy and the Environment*, vol. 32, p. 100405, 2022.

[31] H. Haeri, V. Sarfarazi, A. Hedayat, and Z. M. Zhu, "Numerical simulation of hydraulic fracturing in circular holes," *Computers and Concrete*, vol. 18, no. 6, pp. 1135–1151, 2016.

[32] H. L. Gu, X. P. Lai, M. Tao, W. Z. Cao, and Z. K. Yang, "The role of porosity in the dynamic disturbance resistance of water-saturated coal," *International Journal of Rock Mechanics and Mining Sciences*, vol. 166, p. 105388, 2023.

[33] H. L. Gu, M. Tao, W. Z. Cao, J. Zhou, and X. B. Li, "Dynamic fracture behaviour and evolution mechanism of soft coal with different porosities and water contents," *Theoretical and Applied Fracture Mechanics*, vol. 103, p. 102265, 2019.

[34] H. L. Gu, M. Tao, X. B. Li, W. Z. Cao, and Q. Y. Li, "Dynamic response and Meso-deterioration mechanism of water-saturated sandstone under different porosities," *Measurement*, vol. 167, p. 108275, 2021.

[35] B. X. Li, W. S. Zhu, L. Yang, et al, "Experimental research on propagation mode of 3d hollow crack and material failure strength under hydro-mechanical coupling," *Journal of Central South University*, vol. 50, no. 5, pp. 1192–1202, 2019.

[36] J. W. Fu, W. S. Zhu, X. Z. Zhang, L. Y. Shi, and F. D. Xie, "Fracturing experiment and numerical simulation study on new material containing a hollow internal crack under internal water pressure," *Advanced Engineering Sciences*, vol. 49, no. 4, pp. 78–85, 2017.

[37] J. Mei and W. Z. Zhang, "An experimental and numerical investigation on the initiation and interaction of double cracks in rocks under hydromechanical coupling," *Advances in Materials Science and Engineering*, vol. 2020, p. 8210453, 2020.

[38] J. X. Cao, Z. D. Zhu, Y. Tian, C. Y. Zhao, and X. Q. Dong, "The experimental study of propagation progress of 3d crack-SETS under hydraulic pressure," *Science Technology and Engineering*, vol. 17, no. 4, pp. 92–98, 2017.

[39] K. L. Guo, L. Yang, X. C. Sheng, et al, "Fracture mechanical behavior and AE characteristics of rock-like material containing 3-D crack under hydro-mechanical coupling," *Rock and Soil Mechanics*, vol. 40, no. 11, pp. 4380–4390, 2019.

[40] C. Wei, W. S. Zhu, Y. Li, et al, "Experimental study and numerical simulation of inclined flaws and horizontal fissures propagation and coalescence process in rocks," *Rock and Soil Mechanics*, vol. 40, no. 11, pp. 4533–4542, 2019.

[41] J. Q. Xing, C. Zhao, S. B. Yu, H. Matsuda, and C. C. Ma, "Experimental study on rock-like specimens with single flaw under hydro-mechanical coupling," *Applied Sciences*, vol. 9, no. 16, p. 3234, 2019.

[42] C. Zhao, J. Q. Xing, J. L. Niu, and C. C. Ma, "Experimental study on crack propagation of precrack rock-like specimens under hydro-mechanical coupling," *Chinese Journal of Rock Mechanics and Engineering*, vol. 40, no. 11, pp. 4533–4542, 2019.

[43] L. Yang, J. Mei, X. C. Sheng, W. M. Yang, and J. L. Li, "Cracking and creep behavior of rocks considering propagation and interaction of adjacent cracks under hydro-mechanical coupling," *Rock Mechanics and Rock Engineering*, vol. 54, no. 8, pp. 4099–4110, 2021.

[44] J. Mei, L. Yang, X. C. Sheng, G. X. Song, W. M. Yang, and B. Zhang, "Time-dependent propagation of 3-D cracks in rocks under hydromechanical coupling," *Rock Mechanics and Rock Engineering*, vol. 53, no. 4, pp. 1923–1934, 2020.

[45] J. Mei, L. Yang, X. C. Sheng, X. J. Ma, B. Sui, and W. M. Yang, "An experimental and theoretical investigation of time-dependent cracking and creep behavior of rocks under triaxial hydro-mechanical coupling," *Theoretical and Applied Fracture Mechanics*, vol. 115, p. 103046, 2021.

[46] Q. B. Lin, P. Cao, H. Wang, and R. H. Cao, "An experimental study on cracking behavior of precracked sandstone specimens under seepage pressure," *Advances in Civil Engineering*, vol. 2018, p. 4068918, 2018.

[47] Y. L. Zhao, Q. Liu, H. Liu, et al, "Triaxial compression and acoustic emission tests on single cracked limestone and compression–shear fracture model under hydraulic-mechanical coupling action," *Journal of China Coal Society*, vol. 46, no. 12, pp. 3855–3868, 2021.

[48] S. Luo and F. Q. Gong, "Evaluation of energy storage and release potentials of highly stressed rock pillar from rockburst control perspectives," *International Journal of Rock Mechanics and Mining Sciences*, vol. 163, p. 105324, 2023.

[49] S. Luo, F. Q. Gong, L. L. Li, and K. Peng, "Linear energy storage and dissipation laws and damage evolution characteristics of rock under triaxial cyclic compression with different confining pressures," *Transactions of Nonferrous Metals Society of China*, vol. 33, no. 7, pp. 2168–2182, 2023.

[50] Q. Q. Zheng, J. W. Qian, H. J. Zhang, Y. K. Chen, and S. H. Zhang, "Velocity tomography of cross-sectional damage evolution along rock longitudinal direction under uniaxial loading," *Tunnelling and Underground Space Technology*, vol. 143, p. 105503, 2024.

[51] Q. Wang, D. C. Wang, J. W. Fu, et al, "Effects of particle size and loading rate on the tensile failure of asphalt specimens based on a direct tensile test and particle flow code simulation," *Structural Engineering and Mechanics*, vol. 86, no. 5, pp. 607–619, 2023.

[52] H. Cheng, X. P. Zhou, J. Zhu, and Q. H. Qian, "The effects of crack openings on crack initiation, propagation and coalescence behavior in rock-like materials under uniaxial compression," *Rock Mechanics and Rock Engineering*, vol. 49, no. 9, pp. 3481–3494, 2016.

[53] D. Y. Wu, L. Y. Yu, H. J. Su, et al, "Experimental study and Pfc3D simulation on crack propagation of fractured rock-like specimens with bolts under uniaxial compression," *Rock and Soil Mechanics*, vol. 42, no. 6, pp. 1681–1692, 2021.

[54] M. Sagong and A. Bobet, "Coalescence of multiple flaws in a rock-model material in uniaxial compression," *International Journal of Rock Mechanics and Mining Sciences*, vol. 39, no. 2, pp. 229–241, 2002.

[55] Q. B. Lin, P. Cao, G. P. Wen, J. J. Meng, R. H. Cao, and Z. Y. Zhao, "Crack coalescence in rock-like specimens with two dissimilar layers and pre-existing double parallel joints under uniaxial compression," *International Journal of Rock Mechanics and Mining Sciences*, vol. 139, p. 104621, 2021.

[56] D. G. Aggelis, D. V. Soulioti, N. Sapouridis, N. M. Barkoula, A. S. Paipetis, and T. E. Matikas, "Acoustic emission characterization of the fracture process in fibre reinforced concrete," *Construction and Building Materials*, vol. 25, no. 11, pp. 4126–4131, 2011.

[57] K. Ohno and M. Ohtsu, "Crack classification in concrete based on acoustic emission," *Construction and Building Materials*, vol. 24, no. 12, pp. 2339–2346, 2010.

[58] X. Wang, Q. L. Zou, R. Z. Wang, Z. Y. Li, and T. C. Zhang, "Deformation and acoustic emission characteristics of coal with different water saturations under cyclic load," *Soil Dynamics and Earthquake Engineering*, vol. 162, p. 107468, 2022.